Transp Porous Med (2018) 122:421–436
https://doi.org/10.1007/s11242-018-1014-5

Reversible and Irreversible Tracer Dispersion in an Oscillating Flow Inside a Model Rough Fracture

Yanina Lucrecia Roht[1] · Ricardo Chertcoff[1] · Jean-Pierre Hulin[2] · Harold Auradou[2] · Irene Ippolito[1]

Received: 31 March 2017 / Accepted: 31 January 2018 / Published online: 10 February 2018

Abstract We study the mixing dynamics of a dyed and a clear miscible fluid by an oscillating flow inside an Hele-Shaw cell with randomly distributed circular obstacles. A transparent setup allows us to analyze the distribution of the two fluids and the reversible and irreversible mixing components. At the lower Péclet numbers Pe (based on the averaged absolute fluid velocity), geometrical dispersion due to the disordered flow field between the obstacles is dominant: the corresponding dispersivity is constant with Pe and, at constant Pe, increases with the amplitude of the oscillations and is negligible at small ones. Compared to echo dispersion with only one injection–suction cycle, oscillating flows are shown to provide additional information when the number of oscillations and, as a result, the distance of transverse mixing are varied. Geometrical dispersion is dominant up to a limiting Pe increasing with the amplitude. At higher $Pe's$, the results are similar to those of Taylor dispersion in cells with smooth walls.

Keywords Reversibility · Fracture · Dispersion · Rough · Oscillating

✉ Jean-Pierre Hulin
hulin@fast.u-psud.fr

Yanina Lucrecia Roht
yroht@fi.uba.ar

Ricardo Chertcoff
rchertc@fi.uba.ar

Harold Auradou
auradou@fast.u-psud.fr

Irene Ippolito
i.ippoli@fi.uba.ar

[1] Universidad de Buenos Aires, Facultad de Ingeniería, Grupo de Medios Porosos, Paseo Colón 850, 1063 Buenos Aires, Argentina

[2] Lab. FAST, CNRS, Univ. Paris-Sud, Bât. 502, Campus Univ, 91405 Orsay, France

Oscillating flows in porous media are encountered in many areas of applied science (Leong and Jin 2006; Dey and Raja 2014; Ashorynejad et al. 2016), as well as in our natural environment (Sanz-Prat et al. 2016; Ping Wang 2015). One of the open questions concerns the influence of a time periodic flow on the performance of processes such as thermal or electrical diffusion, species separation or, as in the present study, mass transfer. To our knowledge, relatively little attention has been paid to the effect of oscillating flows on the dynamics of the spreading of concentration fronts. Apart from references Scotter et al. (1967), Scotter and Raats (1968) and Cirkel (2015) dealing, respectively, with the dispersion of a gas inside another one and with nonlinear exchange processes, most studies consider very simple geometries like parallel planes or Hele-Shaw cells with plane walls (Watson 1983; Roht et al. 2015).

Mixing and dispersion in porous media are controlled by the interplay between convection and molecular diffusion of the solute. The Péclet number $Pe = UH/D_m$ characterizes the relative weight of the two processes (U is the average flow velocity, H the characteristic microscopic length of the medium, and D_m the molecular coefficient of diffusion of the solute). The different dispersion regimes are presently well understood in the case of a constant fluid flow. Several mechanisms have been identified: for $Pe < 1$, mixing is controlled by molecular diffusion. At larger Pe values, the disorder of the pore space and the spatial correlation of the velocity of the tracer particles along the trajectories are the key elements influencing dispersion (Saffman 1959; Fried 1971; Bear 1972): this mechanism is often referred to as geometrical dispersion and its contribution to the dispersion coefficient is proportional to Pe. In the particular case of flow between two continuous walls (like inside fractures of rocks or building materials), Taylor dispersion is generally dominant at large Péclet numbers (Boschan et al. 2008) with a contribution to the dispersion coefficient proportional to Pe^2: it reflects an equilibrium between tracer spreading due to the flow velocity gradient perpendicular to the walls and transverse molecular diffusion across the gap (Taylor 1953; Aris 1956). However, natural fractures have generally rough walls: then, in this case, the flow field is disordered due to fluctuations of the fracture aperture and geometrical dispersion is again dominant at low Péclet numbers (Ippolito et al. 1994; Roux et al. 1998).

Oscillations (with zero mean displacement) introduce two new characteristic parameters: the amplitude A and the period T of the displacement. For dispersion in an oscillating flow between smooth parallel walls, Watson (1983) and Roht et al. (2015) have shown that Taylor dispersion can develop only if the ratio τ_m/T is below a threshold value ($\tau_m = H^2/D_m$ is the characteristic diffusion time between the walls and H is the distance between them). In this case, the dispersivity $l_d = D/U$ is proportional to the amplitude A and $l_d/A \propto \tau_m/T$. At higher values of τ_m/T, spreading is still diffusive macroscopically, but l_d/A varies instead as $(\tau_m/T)^{-1}$. This is due to a partial reversibility of the process: after a change of the flow direction, spreading initially decreases instead of continuing to increase as is the case for low values of τ_m/T. However, the average over several periods of the variation is still increasing.

While Taylor dispersion in oscillating flows in simple geometries is now well understood, little is known on the influence of flow oscillations on the geometrical dispersion mechanism. Dispersion measurements in oscillating gas flows of zero mean value inside random sphere packings have been reported by Scotter et al. (1967) and Scotter and Raats (1968): these authors showed that both the Péclet number and the normalized amplitude of the oscillations had a major influence on the dispersion coefficient. However, due to experimental limitations, their study is restricted to small amplitudes with respect to the size of the spheres and to long periods. These authors adapted Saffman's theory to unsteady flows, but theoretical laws obtained in this way did not fit fully the experimental data. They explained this difference (Raats 1969; Nowamooz et al. 2013) by memory effects due to the incomplete diffusive

homogenization of concentration gradients induced by the flow before its reversal. This leaves open the problem of the scaling laws followed by the dispersion coefficient as a function of the control parameters of the flow, particularly for large amplitudes of the displacement which are of interest in the present work.

The objective of the present work is to investigate experimentally these issues by using optical dispersion measurements of tracer dispersion in oscillating flows inside a transparent model representing a rough fracture. This allows us to study both the spatial distribution of the tracer in the model and its variation with time during the oscillations of the flow. The scaling laws satisfied by the dispersion process and the different dispersion mechanisms at work will now be investigated from measurements taken in a broad range of Péclet numbers and oscillation periods and amplitudes.

1 Experimental Setup and Procedure

Like previous works by these authors and by Boschan et al. (2008) and Nowamooz et al. (2013) using stationary flows, the experiments were performed in a transparent model of rough fractures. It has the geometry of a Hele-Shaw cell of length and width, respectively, equal to 400 and 50 mm (i.e., similar to those of the cell used by Roht et al. (2015)). The cell contains 2372 circular obstacles of height $H = 0.42$ mm equal to the cell gap (see Fig. 1) and distributed at random in the gap: the diameter of the obstacles is $d = 1.4$ mm and the minimum and mean values of the distance between their centers are, respectively, 2.1 and 2.4 mm. The layout of the obstacles is generated by computer, and they cover 20% of the area of the cell walls: the latter are carved on plexiglas blocks by means of a computer-controlled milling machine. One of the walls is plane, and the obstacles protrude out of the other: the two walls are then assembled with the top of the obstacles in contact with the smooth plane wall.

The fluids used in the experiments are aqueous solutions of glycerol with a relative mass concentration of 21% and a viscosity $\mu = 1.8$ mPa s (at 22 °C). All the experiments were performed at a constant temperature of 22 °C. Water Blue dye (Horobin and Kiernan 2002) at

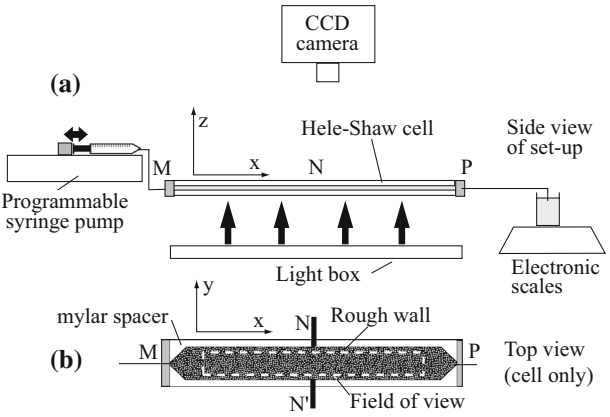

Fig. 1 Schematic views of the Hele-Shaw cell and of the global experimental setup. **a** Side view, **b** top view. The rectangle bounded by a dashed white line corresponds to the field of view of the images used in the analysis

a concentration of 2.0 g/l is added to one of the solutions as a passive tracer. The molecular diffusion coefficient D_m of the dye, as determined through independent measurements and from the literature (Charette et al. 2007; Russel et al. 1995), is $D_m = 4.06 \times 10^{-4}\,\mathrm{mm}^2/\mathrm{s}$ for the 21% glycerol solution. The characteristic diffusion time across the cell gap is then: $\tau_m = H^2/D_m = 434\ s$.

During the experiments, the inlet M of the cell is connected to a NEMESYS™ programmable syringe pump. Both the driving system of the pump and the syringe can work in the injection and suction modes, i.e., fluid can be made to flow either into or out of the syringe. This allows to generate oscillating flows of zero time-averaged flow rate. Before the experiments, the empty cell is first placed vertically and a flow of CO_2 is imposed between M and P (Fig. 1). Once the cell is saturated, CO_2 is replaced by water which is also circulated between M and P. Trapped CO_2 bubbles get quickly dissolved into the water which allows for a full saturation of the cell with liquid.

Then, the dyed and clear fluids are injected separately at a same constant rate (0.5 ml/min), respectively, through ports M and P and flow together out of the cell through ports N and N' at equal flow rates. The symmetry of this setup (and, therefore, of the flow field) insures that each half of the cell is saturated with one of the fluids and separated from the other by a straight front (Fig. 2a): its deviation from a straight line is of the order of the radius of an obstacle (0.7 mm). The local thickness remains of the order of 0.5 mm (Fig. 2d) due to the flow of the fluid toward the sides which limits broadening by molecular diffusion due to the finite transit time of the fluid particles along the front.

After the saturation of the cell, a flow rate varying sinusoidally is applied at the inlet M. For a given setting of pump, the amplitude of the oscillations of the fluid may be estimated from the cross section of the cell transverse to the flow and from manufacturer's data on the calibration of the pump for a given type of syringe: in this work, A ranges from 2 to 40 mm. This latter upper value is set by the length and the need to keep at all times the whole front

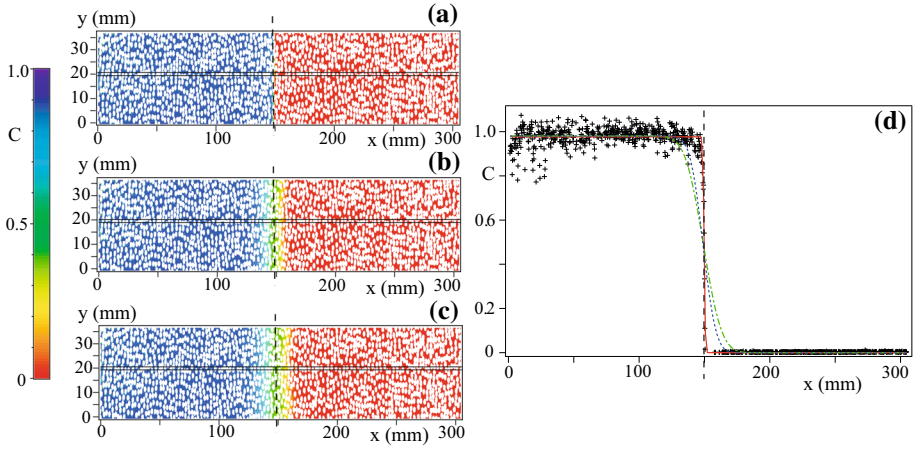

Fig. 2 Maps of the relative concentration $C(x, y, t)$ at different times $t_1 = 0$ (**a**), $t_2 = 10T = 80$ s (**b**) and $t_3 = 20T = 160$ s (**c**) during an experiment with $T = 8$ s and $A = 8$ mm ($t = 0$ is the time at which the pump is started). Color scale at the left: relative concentration C (red: $C = 0$; blue: $C = 1$). Obstacles appear in white (their elliptical shape on the graph is due to different magnifications in the x and y directions). **d** Variations with x of the average of $C(x, y, t)$ over the interval of y values defined by parallel black lines in Figs. (a,b,c) at times $t_1 = 0$: (+) symbols and continuous red curve, t_2 and t_3: respectively, black dotted and green dashed-dotted curves. Vertical dashed lines in all graphs: initial mean location of the front

inside the cell. For checking these values of A, the outlet P of the cell is connected to a beaker placed on a scale of resolution ± 0.01 mg. The total variations of weight corresponding to the fluid volume swept by the displacement A range between 35 and 700 mg and are, therefore, measured precisely by the scale. The amplitude A determined in this way is equal within 5% to the first estimations, and its variation with time is well fitted by a sine wave.

Since, by definition, the average over the section of the displacement of the fluid varies with time as $A\ \sin(\omega t)$ with $\omega = 2\,\pi/T$, the corresponding mean fluid velocity at the time t is:

$$\langle v_x(y,z,t)\rangle_{y,z} = \omega\, A\ \cos(\omega\, t) = (\pi/2)\, U\ \cos\ (\omega\, t)\,. \tag{1}$$

$U = 4A/T$ is selected as the characteristic velocity of the oscillating flow because it represents the average of the *absolute* value of $\langle v_x(y,z,t)\rangle_{y,z}$ over an oscillation period (the maximum mean velocity during a period is $\pi\, U/2$).

The cell is illuminated from below, and the relative concentration field $C(x, y, t)$ is determined from images acquired by a digital CCD camera (Roper Coolsnap FX) located above the cell as described by Roht et al. (2015), Boschan et al. (2007, 2008) and Charette et al. (2007). C is the concentration of dye averaged over the gap H of the cell and divided by its value for the pure dyed solution (C varies therefore between 0 and 1). The images used in the following for the analysis are regions of interest of size 1250×152 pixels inside the full field of the camera and correspond to a field of view of 305×37 mm (the resolution of the image is 4.1pixels/mm). In order to reduce interpretation errors due to wall effects, two bands with a width of 2.5 mm each are removed at both sides parallel to the flow of the image of the cell. For each experiment, a set of 20 images is acquired during each oscillation. Typical maps of the relative concentration at different times (starting with $t = 0$) are shown in Fig. 2a–c, together with a profile of its variation with the distance x parallel to the flow (Fig. 2d).

For characterizing the heterogeneity of the model fracture, we performed experiments (referred to in the following as 'transmission" ones) in which the fluid flows always in the same direction at a constant velocity. The tracer concentration is measured by the same optical technique as for oscillating flows and is expected to follow the classical convection-diffusion equation:

$$\frac{\partial C}{\partial t} + U\frac{\partial C}{\partial x} = D\frac{\partial^2 C}{\partial x^2}. \tag{2}$$

For a step like injection, the analytical solution is:

$$C(x,t) = \frac{1}{2}\left[1 - \mathrm{erf}\left(\frac{x - \bar{x}(t)}{\sqrt{2\,\overline{\Delta x^2}(t)}}\right)\right], \tag{3}$$

where $\bar{x}(t) = Ut$ is the average front location and $\overline{\Delta x^2} = \left\langle (x - \bar{x})^2 \right\rangle = 2Dt$ characterizes the width of the front. For given values of the transverse distance y and of the time t, the profiles $C(x, y, t)$ have been fitted from Eq. (3) by adjusting the two parameters $\bar{x}(y)$ and $\overline{\Delta x^2}(y)$ using a least squares method. The averages of these two parameters with respect to y provides the mean front location $\bar{x}(t)$ and the mean square width $\overline{\Delta x^2}(t)$.

A typical variation of $\overline{\Delta x^2}(t)$ with time is shown in the insert (a) of Fig. 3 (continuous line). After an initial transient phase, $\overline{\Delta x^2}(t)$ increases globally linearly with time. The dispersion coefficient D is equal to half the slope of this curve in an interval Δt inside this long time limit so that the dispersivity $l_d^{\mathrm{trans}}(t) = D/U$ satisfies:

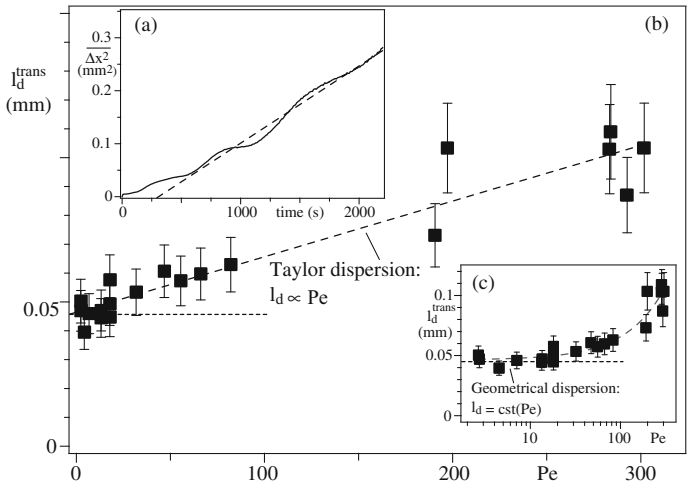

Fig. 3 **a** Variation of $\overline{\Delta x^2}$ with time t (continuous line) for a "transmission" dispersion measurement during which the direction of the flow is kept constant ($Pe = 18$). Dashed line: linear fit at long times from which the dispersivity l_d^{trans} is computed by means of Eq. (4). **b**, **c** Variation of l_d^{trans} with Pe in linear coordinates (**b**) and for a logarithmic horizontal scale (**c**). Dashed lines: fit with a linear variation of l_d^{trans} with Pe; dotted lines: limiting value at $Pe = 0$. Error bars: see explanation in the description of the data analysis in Sect. 1

$$l_d^{\text{trans}}(t) = \frac{\Delta(\overline{\Delta x^2}(t))}{2\,U\Delta t} = \frac{\Delta(\overline{\Delta x^2}(t))}{2\,\Delta(\bar{x}(t))}. \tag{4}$$

Each experiment has been repeated three times for a same set of control parameters. The corresponding values of l_d are then averaged and plotted in the graphs. We estimated the relative error by computing for each set of control parameters the maximum difference between the corresponding values of l_d and dividing by the mean value. For all data sets $\pm 15\%$ has appeared as a maximum of the relative error and this value is, therefore, used to estimate the errors in the rest of the paper. Error bars corresponding to these values are shown in Fig. 3b, c.

The experimental variation of l_d^{trans} with the Péclet number is shown in Fig. 3b, c. From previous experiments in similar systems (Ippolito et al. 1994; Boschan et al. 2008) and taking into account the fact that pure molecular diffusion is negligible, l_d^{trans}/H may be expected to vary with the Péclet number like:

$$\frac{l_d^{\text{trans}}}{H} = \frac{D}{UH} = \alpha_G + \alpha_T Pe. \tag{5}$$

The first term corresponds to the geometrical dispersion mechanism ($l_d = cst(Pe)$) and the second one to the Taylor dispersion one ($l_d \propto Pe$). A good fit of Eq. 5 with the experimental values is obtained for $\alpha_G = 1.10 \pm 0.03$ and $\alpha_T = 0.0046 \pm 0.001$ (dashed lines in Fig. 3b, c): geometrical dispersion is dominant (and $l_d \simeq cst(Pe)$) for $Pe \lesssim 30$ while Taylor dispersion is dominant at higher Péclet numbers. One notes that the experimental value of α_T is close to the analytical value for flow between parallel walls ($1/210 \simeq 0.00476$).

In the following section, we report dispersion measurement results obtained with oscillating flows and compare them to the above transmission measurements and to those of echo experiments in which the fluid is first injected into the model and then sucked back at the same absolute velocity.

2 Experimental Results

2.1 Front Width Variations Induced by an Oscillating Flow

When the flow rate oscillates with a period T, the mean square front width $\overline{\Delta x^2}$ still increases globally linearly with time over long time intervals $\Delta t \gg T$, but oscillations are superimposed onto the linear trend (main graph and insert of Fig. 4). The mean front displacement $\overline{\delta x(t)}$ varies sinusoidally with the motion of the pump (dashed blue curve in the insert); note that the pump is set so that, at $t = 0$ or $t = NT$ (N integer), $\overline{\delta x(t)}$ is maximum.

When the direction of the flow is reversed (both at $t = T = 8$ s and $t = 3T/2 = 14$ s), the width $\overline{\Delta x^2}$ of the mixing front starts to decrease after having increased before the reversal. This shows that the interpenetration of the two fluids is reduced by the reversal of the flow and is therefore partly reversible: this trend lasts for a quarter period or so (intervals 2 and 4). Then, during interval 3 before the next reversal, $\overline{\Delta x^2}$ increases again. These alternate zones of positive and negative slope are visible at all distances in the main graph. The origin of the partial reversibility is discussed in more detail in Sect. 2.3. By analogy with transmission experiments, an oscillating flow dispersivity is defined by:

$$l_d^{\mathrm{osc}} = \overline{\Delta x^2}/2\,x_{tr}. \tag{6}$$

Like for transmission experiments, this ratio varies with x_{tr}, particularly at short distances but reaches asymptotically a limit at large distances x_{tr}. We study first the variation of this limit with the experimental parameters, and the dependence of l_d^{osc} on x_{tr} will be discussed in Sect. 2.3.

2.2 Influence of Wall Roughness on Dispersion in Oscillating Flows

In order to investigate the influence of the obstacles on the characteristics of Taylor dispersion, we first compare the present results to those for an Hele-Shaw cell with smooth walls (Roht et al. 2015). Subsequently, we compare the variation with Pe of l_d^{osc}/H for oscillating flows to

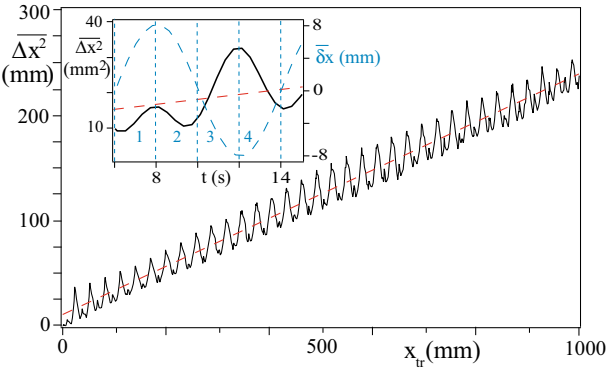

Fig. 4 Variation of $\overline{\Delta x^2}$ with the travelled distance x_{tr} for $A = 8$ mm and $T = 8$ s ($U = 4A/T \sim 4$ mm s^{-1}, $Pe = 4100$ and $\tau_m/T = 54$). Dashed red line: linear variation for $l_d^{\mathrm{osc}} = (1/2)\overline{\Delta x^2}/x_{tr} = 0.121$ mm ($l_d/A = 0.0151$). Insert: enlarged view of the variations with time of $\overline{\Delta x^2}$ (continuous curve) and of the front displacement $\overline{\delta x(t)}$ from its mean location (blue dashed curve). Vertical dotted lines: times corresponding to (from left to right): $t = 3T/4, T, 5T/4, 3T/2, 7T/4$

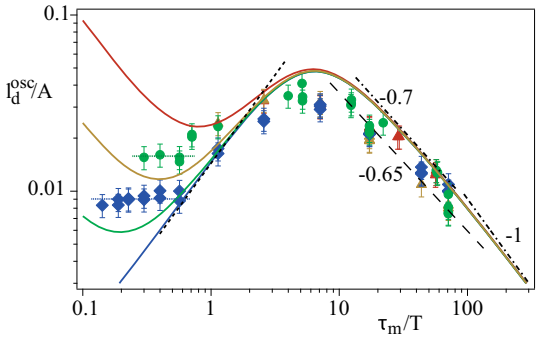

Fig. 5 Variation of the normalized dispersivity l_d^{osc}/A as a function of $\tau_m/T = H^2/(D_m T)$. Oscillating flows of amplitudes: $A = 2$ mm (▼); $A = 4$ mm (▲); $A = 8$ mm (●); $A = 40$ mm (♦). Solid lines: analytical predictions (Watson 1983) in smooth fractures for the same values of A (the colors correspond to those of the symbols). Dotted line: slope 1 for the Taylor regime. Dashed-dotted lines: slopes -1 ($Pe \gtrsim 200$) and -0.7 ($10 \lesssim Pe \lesssim 70$) for the partly reversible Taylor regime (analytical values). Dashed line: slope of the trend of the experimental data ($10 \lesssim Pe \lesssim 70$). Horizontal dotted lines: geometrical regimes for $A = 8$ and $A = 40$ mm. Error bars: see Sect. 1

the results of transmission dispersion measurements. We determine, in this way, the influence of the oscillations on the geometrical dispersion at low Pe's.

Partly Reversible and Classical Taylor Dispersion Regimes

For $\tau_m/T \gtrsim 8$, l_d^{osc}/A is predicted analytically (Watson 1983) and numerically (Roht et al. 2015) to decrease as τ_m/T increases unlike for classical Taylor dispersion (Fig. 5). In this regime, the period T is too short compared to τ_m to allow for the diffusion of the tracer across the gap, while the orientation of the flow remains the same. Tracer spreading is still induced by the transverse velocity gradients inside the gap, but its partial reversibility after flow reversals reduces l_d. In this partly reversible Taylor dispersion regime, this result may be retrieved by the following scaling argument (Roht et al. 2015). During a half period, tracer diffuses over a transverse distance $\Delta z \sim \sqrt{D_m T} < H$: multiplying by the transverse velocity gradient estimated by $A/(TH)$ and by the period T provides the order of magnitude $\Delta x \sim A\sqrt{D_m T}/H$ of the irreversible increase in the local front width during the period T. On the other hand, Δx must also be of the order of $\sqrt{DT}$: which leads to the estimate $DT/A^2 = l_d/A \sim (\tau_m/T)^{-1}$.

From this prediction, in the case of smooth walls, the values of l_d^{osc}/A corresponding to different amplitudes collapse onto a single decreasing trend for $\tau_m/T \gtrsim 20$ when plotted as a function of τ_m/T (continuous curves in Fig. 5). We have plotted in this same figure the data obtained in the present work for a rough fracture at different amplitudes: for $\tau_m/T \gtrsim 3$, these points collapse onto a curve similar to the theoretical predictions but with 20% lower values. The slope of this curve is: -0.65 ± 0.05 (dashed line) in the range $10 \lesssim Pe \lesssim 70$ to be compared with -0.7 for the analytical curves.

Geometrical Dispersion Regime

For $\tau_m/T \lesssim 0.7$, instead, l_d^{osc}/A no longer follows these analytical predictions for $A = 8$ and 40 mm: we discuss now this new regime. Figure 6 compares the dispersivities l_d^{osc} from

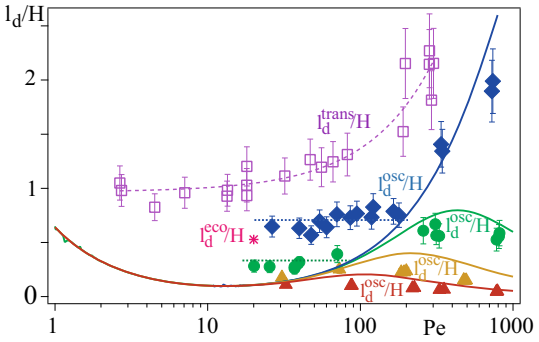

Fig. 6 Variations of l_d/H as a function of the Péclet number $Pe = UH/D_m$ for transmission, echo and oscillating flow experiments. Dark symbols: l_d^{osc}/H for oscillating flows of amplitudes: $A = 2$ mm (▼); $A = 4$ mm (▲); $A = 8$ mm (●); $A = 40$ mm (◆). Error bars: see Sect. 1. Solid lines: analytical predictions (Watson 1983) in fractures with smooth walls for the same values of A. Dotted horizontal lines: geometrical dispersion regime for $A = 8$ and $A = 40$ mm. (⋆) symbol: value of l_d^{eco}/H from echo measurements for $t = 2T_{inv}$ and $x_{tr}/d = 150$ (see Sect. 2.3). (□) symbol: dispersivity l_d^{trans}/H for transmission experiments. Dashed line: adjustment of the transmission data by $l_d^{trans}/H = \alpha_G + \alpha_T Pe$ with $\alpha_G = 1.10 \pm 0.03$ and $\alpha_T = 0.0046 \pm 0.0005$

the same oscillating flow experiments as in Fig. 5 and l_d^{trans} from the "transmission" experiments discussed in Sect. 1: in order to make this comparison possible, l_d^{osc}/H is plotted as a function of the Péclet number: $Pe = UH/D_m = 4AH/(D_m T)$. The analytical predictions for oscillating flows between smooth walls (Watson 1983) are also plotted in the graph (continuous curves). Only data corresponding to the lower range of Péclet numbers are shown. One observes for $A = 8$ and 40 mm, at the lowest Péclet numbers explored, a domain where l_d^{osc}/H is constant with Pe (and, therefore, with T). For $A = 40$ mm, $l_d^{osc}/H = 0.72 \pm 0.08$ ($20 \leq Pe \leq 200$) and, for $A = 8$ mm, $l_d^{osc}/H = 0.29 \pm 0.04$ ($20 \leq Pe \leq 80$). At lower amplitudes $A = 2$ and 4 mm, the geometrical regime is not visible.

These results imply that Eq. (5) becomes:

$$\frac{l_d^{osc}(A, Pe)}{H} = \alpha_G(A) + \alpha_T\, Pe, \tag{7}$$

in which α_G depends on the amplitude A (but not on T or Pe), while, from the previous section, α_T may still be assumed to be constant. The analytical curves of Fig. 6 display a region of negative slope below $Pe \simeq 10$ corresponding to a dominant influence of pure molecular diffusion for smooth fractures: all data obtained for oscillating were obtained at higher values of Pe so that Eq. 7 remains valid. Figure 6 shows that, in the geometrical dispersion regime, l_d/H increases strongly with the amplitude A of the oscillations (this effect will be discussed below).

2.3 Reversibility of Geometrical Dispersion and Large-Scale Heterogeneities

Echo Dispersivity Measurements

The lower value of the dispersivity l_d^{osc} compared to l_d^{trans} suggests that there is a partial reversibility of the dispersion with respect to the reversals of the flow during the oscillations. This is reminiscent of "dispersion echo" measurements in $3D$ porous media in which tracer is injected into the samples and then sucked back through the inlet where the tracer concentration

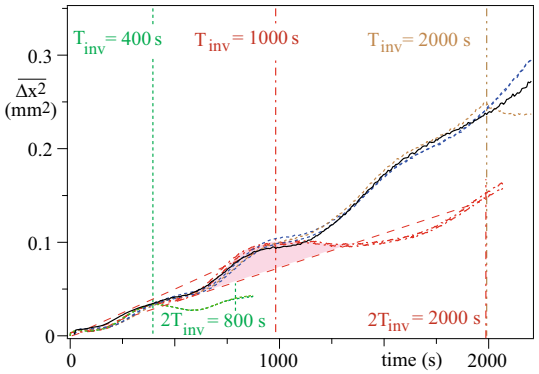

Fig. 7 Variations of the mean square front width $\overline{\Delta x^2}$ as a function of time for dispersion echo experiments corresponding to $Pe = 20$ and to: $T_{\text{inv}} = 400$ s (green curve), $T_{\text{inv}} = 1000$ s (red), $T_{\text{inv}} = 2000$ s (brown) and $T_{\text{inv}} = 5000$ s (blue). Two experimental curves are shown for each of the inversion times $T_{\text{inv}} = 1000$ and 5000 s in order to demonstrate the repeatability of the experiment. Black curve: transmission experiment performed at $Pe = 18$. Dispersivities at T_{inv} (injection) and $2\,T_{\text{inv}}$ (echo) are computed from the slopes of the two dashed lines (shown for $T_{\text{inv}} = 1000$ s)

is measured (Hulin and Plona 1989). In these experiments, the relative values of the echo and transmission dispersivities were shown to depend on the heterogeneities of the permeability field.

In order to investigate the partial reversibility of the dispersion and its relation to flow heterogeneities, we took such echo dispersion measurements in which the absolute flow rate is constant with time and is the same in the injection and suction phases. The measurement of the concentration is again taken optically, and the initial location of the front is the same as for oscillating flow and transmission measurements. All these experiments are performed at $Pe = 20$ ($U \sim 0.019$ mm s^{-1}) corresponding to the geometrical regime; we investigated the influence of the amplitude of the displacement of the front by varying the duration T_{inv} of the injection phase.

Figure 7 displays the variations of $\overline{\Delta x^2}$ as a function of time in several echo experiments corresponding to flow reversal times T_{inv}: the fluid is injected between $t = 0$ and T_{inv} and sucked back between T_{inv} and $2T_{\text{inv}}$. As expected, the variations corresponding to different values of T_{inv} overlay well for $t < T_{\text{inv}}$ and get separated with a lower value when $t > T_{\text{inv}}$. In the injection phase, all curves remain close to that (in black) corresponding to a transmission experiment (black curve) at a similar Péclet number ($Pe = 18$).

For $T_{\text{inv}} = 1000$ s (red curve), for instance, $\overline{\Delta x^2}$ increases initially approximately linearly before displaying an upward bump (pink shade) above $t \sim 2\,T_{\text{inv}}/3$. After the flow inversion, this additional component disappears and one retrieves the initial linear trend above $t \sim 4\,T_{\text{inv}}/3$. Therefore, at the time $t = 2T_{\text{inv}}$ at which the front has moved back to its initial position, the mean square width $\overline{\Delta x^2}(2\,T_{\text{inv}})$ reflects purely irreversible dispersion; for $t = T_{\text{inv}}$, instead, $\overline{\Delta x^2}(T_{\text{inv}})$ combines reversible and irreversible contributions. The corresponding dimensionless dispersivities l_d^{eco}/d (□) and l_d^{inj}/d (◯) are plotted in Fig. 8 as a function of the respective dimensionless travelled distances $x_{tr}/d = 2UT_{\text{inv}}/d$ and UT_{inv}/d.

Both l_d^{inj}/d and l_d^{eco}/d increase with distance, as could be expected from the upward curvature of the curves of Fig. 7. Moreover, l_d^{eco}/d is always significantly lower than l_d^{inj}/d. In view of the type of variation of l_d^{eco}/d an l_d^{inj}/d with x_{tr} and in spite of the small number

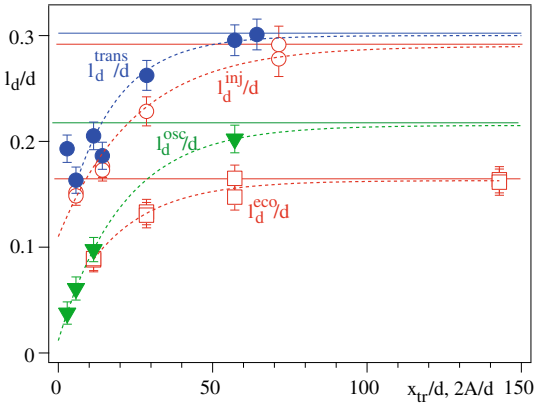

Fig. 8 **a** (▼): variations with $2A/d$ of the limiting value of l_d^{osc}/d at long times at $Pe = 20$. (◯), (□) and (●): respective variations of the dispersivities l_d^{inj}/d, l_d^{eco}/d and l_d^{trans} with the dimensionless travelled distance x_{tr}/d. Dotted lines: fits by exponential variations: $l_d^{\mathrm{trans}}/d = 0.31 - 0.19\exp(-x_{tr}/(18d))$, $l_d^{\mathrm{inj}}/d = 0.29 - 0.18\exp(-x_{tr}/(25d))$, $l_d^{\mathrm{eco}}/d = 0.17 - 0.13\exp(-x_{tr}/(19.5d))$ and $l_d^{\mathrm{osc}}/d = 0.215 - 0.20\exp(-2A/(20.8d))$. Horizontal lines: limits of the dispersivities at large values of A/d and x_{tr}/d. Error bars: see Sect. 1. Dispersivity values l_d^{osc} plotted in the figure correspond to long time limits

of data points available, we attempted to determine a characteristic distance of this variation by fitting it by an exponential relaxation toward an asymptotic value. The results of the fit (see caption of Fig. 7) lead to characteristic distances, respectively, equal to $x_{tr} = 25 \pm 5\,d$ and $19.5 \pm 4\,d$ (the relative error on the relaxation distance is of the order of $\pm 20\%$).

As expected, the variation of l_d^{inj}/d is similar to that of l_d^{trans}/d (●). The difference between the limiting values at the largest x_{tr} (0.291 and 0.302) is within the error bars (see Sect. 1), and the differences between their variations with x_{tr} are also within these error bars except for $x_{tr} \sim 30$ where they are slightly outside. Both values are significantly larger than the asymptotic limit $\simeq 0.17\,d$ of l_d^{eco}. There remains therefore, even at large distances, a large reversible contribution to dispersion which can be characterized by the ratio $l_d^{\mathrm{eco}}/l_d^{\mathrm{inj}} \simeq 0.65$.

Comparing echo and transmission dispersion in heterogeneous and stratified porous media (Hulin and Plona 1989; Leroy et al. 1992) provided similar results which were accounted for by permeability heterogeneities of size larger than the characteristic microscopic length. In order to determine whether such heterogeneities are present here, we estimate now the velocity field from the time dependence of the tracer concentration distribution in the echo experiments.

Flow Heterogeneities and Channelization in the Model Fracture

For estimating the flow field $v_x(x, y)$, we used the map, in the (t, y) plane, of the first moment $\bar{x}(t, y)$ of the distribution of the tracers at a time t and a transverse distance y. For a pair of values (t, y), the ratio $(\bar{x}(t + \Delta t, y) - \bar{x}(t, y))/\Delta t$ provides an estimation of the velocity component v_x at the time $(t + \Delta t)/2$ and at the point of coordinates $((\bar{x}(t + \Delta t) + \bar{x}(t))/2, y)$. Since the velocity component $v_x(x, y)$ is constant with time during either the injection or the suction phase, one obtains, in this way, velocity maps for each phase. Such maps computed at the end of the injection phase is shown in Fig. 9a, b for $T_{\mathrm{inv}} = 1000$ and 2000 s, respectively.

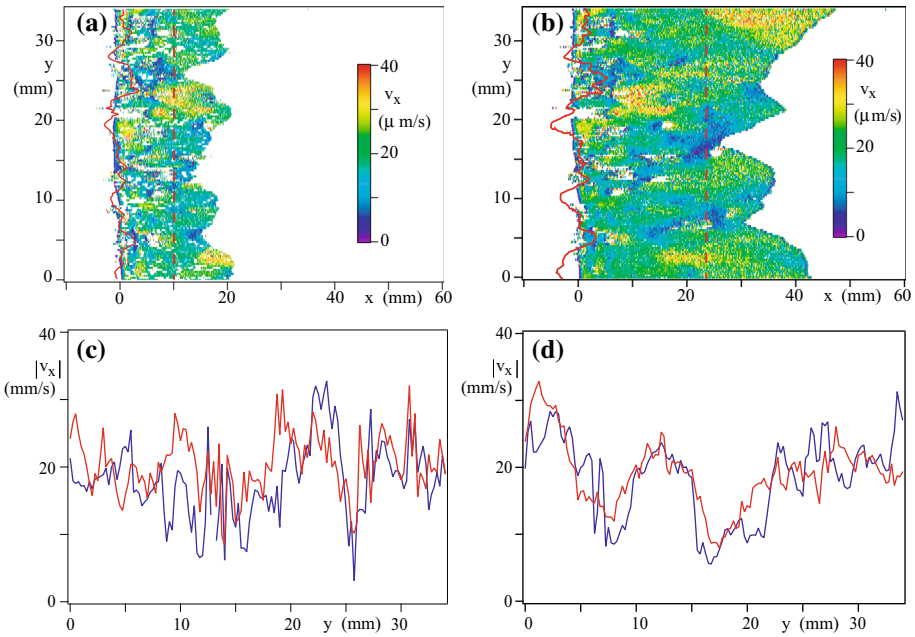

Fig. 9 Maps of the estimated local velocity component v_x (see color scale) of the front at the end of the injection phase ($t = T_{\text{inv}}$) of two echo experiments with $T_{\text{inv}} = 1000$ s (**a**) and 2000 s (**b**) (Fig. 7). Continuous red curve at left of the maps: front contour at $t = 2\,T_{\text{inv}}$. The scales in the x and y directions are different. **b** Transverse profiles of the absolute front velocity component $|v_x|$ across the width of the cell at distances $x = 10$ mm (**c**) and 24 mm (**d**) [vertical red dashed lines in (**a**) and (**b**)] during the injection (blue curve) and suction (red curve) phases [respectively, for maps (**a**) and (**b**)]

The zones where data points are available are bounded to the left by the initial location of the front and to the right by its contour at $t = T_{\text{inv}}$.

Figure 9a, b shows macroscopic regions of low velocity (in blue) and high velocity (in yellow-red), with a width ΔW of the order of 10 mm marked, respectively, by troughs and peaks in the geometry of the fronts. As expected, similar regions are found in graphs (a,b) at distances $\lesssim$ 15 mm appearing in both graphs. Also, the amplitude of the troughs and peaks of the front is significantly larger in graph (b) than in (a), due to its development. These macroscopic spatial variations of the velocity are confirmed by the transverse velocity profiles obtained at $x = 10$ and 24 mm and in Fig. 9c and d: the amplitude of these velocity variations is comparable in both graphs. For a same value of T_{inv}, these profiles are also similar in the injection and suction phases (blue and red curves): this supports the assumption of a reversibility of the macroscopic flow structure. The continuous red lines at the left of maps (a) and (b) correspond to the contour of the front at the end of the suction phase at $t = 2\,T_{\text{inv}}$: in both cases, although the lines are broader than the initial front (left border of colored area), their width is smaller than at the end of the injection phase (right border).

The macroscopic high and low velocity channels observed in Fig. 9 induce large-scale distortions of the displacement front which are partly reversible when the flow direction is reversed. These channels may therefore account for the difference between l_d^{inj}/d and l_d^{eco}/d observed in the experiments. Similar channels were also observed in other types of model fractures (Boschan et al. 2007) and put in evidence in natural fractures by field experiments.

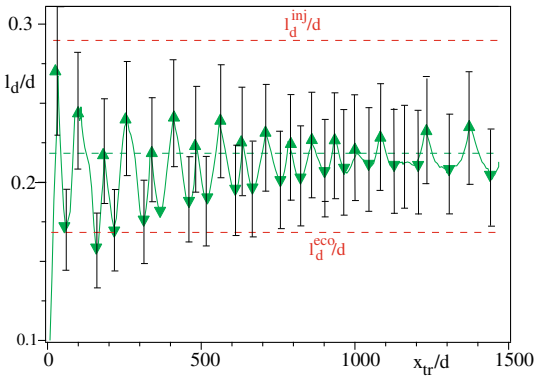

Fig. 10 Variation of the instantaneous dimensionless dispersivity $l_d/d = \overline{\Delta x^2}(t)/(2x_{tr}(t)\,d)$ as a function of $x_{tr}(t)$ (continuous green line) for the oscillating flow experiment corresponding to $Pe = 20$ and $2A/d = 57$. (▲) and (▼): respective maxima and minima of the continuous curve. Horizontal dashed red lines: asymptotic values at large x_{tr}/d of l_d^{inj}/d (upper line) and l_d^{eco}/d (lower line) in Fig. 8. Horizontal dashed green line: asymptotic value of l_d^{osc}/d in Fig. 8. Error bars: see Sect. 1

Comparing Dispersivities in Echo and Oscillating Flow Experiments

The variations of l_d^{eco}/d and of l_d^{osc}/d, respectively, with x_{tr} and $2A$ provide complementary information on the influence of the distance explored by the front. In echo experiments, indeed, the total distance travelled x_{tr} is always twice the amplitude of the motion of the front. In oscillating flows, instead, the travelled distance is $4\,A\,N$ in which N is the number of periods of oscillation: for a same Péclet number Pe and global amplitude $2A$ of the front displacement, one may therefore still increase x_{tr} by increasing N. The dispersivity l_d^{osc}/d for N large enough to reach a constant asymptotic value of l_d^{osc} is plotted in Fig. 8 as a function of the dimensionless parameter $2A/d$ ($2A/d$ is used in the plot instead of A/d because it represents the global displacement of the front).

The variation of l_d^{osc}/d with $2A/d$ is qualitatively close to those of l_d^{eco}/d or l_d^{inj}/d with x_{tr}/d: it can be fitted by an exponential relaxation with a similar characteristic length $\simeq 20.5\,d$. The limiting dispersivity at long distances $l_d^{osc} \simeq 0.215\,d$ is intermediate between l_d^{eco} and l_d^{inj}.

A remaining important issue in the oscillating flow experiments is the influence of the number N of oscillations on the dispersivity l_d^{osc}/d. It is analyzed in Fig. 10 by plotting the local maxima (▲) and minima (▼) of the variation of l_d^{osc}/d as a function of x_{tr}. The experiment is that corresponding to the rightmost (▼) symbol in Fig. 8. At short times, i.e., after one or two oscillations, the maximum and minimum values are quite different. They are, respectively, of the same order of magnitude as l_d^{inj} and l_d^{eco} for similar travelled distances (red dashed lines). This was to be expected since the variation of the flow with time during one period is similar to that during an echo experiment: however, this variation is a sine wave instead of a square one which may account for the small differences of the values. At large distances x_{tr} the amplitude of the oscillations is reduced and the mean value (averaged over a period) corresponds to that plotted in Fig. 8 (green horizontal dashed line).

3 Discussion–Conclusion

The experiments discussed above have shown that dispersion in oscillating flows inside a Hele-Shaw cell with obstacles is controlled by geometrical dispersion at low Péclet numbers and by normal or partly reversible Taylor dispersion at high ones. The transition between the two regimes takes place at a Péclet number increasing with the amplitude A of the oscillations and the geometrical regime is only visible above a minimum amplitude A ($\sim$ 8 mm). In contrast to low Pe's (no geometrical dispersion occurs in smooth cells), results at high $Pe's \gtrsim 200$ are well accounted for by models and simulations developed for smooth cells (Watson 1983). The agreement is better in the partly reversible Taylor and transition regimes ($\tau_m/T \gtrsim 3$) where the dispersivities are only 20% lower than the numerical ones. Classical, irreversible, Taylor dispersion is only fully established in smooth cells (Roht et al. 2015) for $\tau_m/T \lesssim 2$ and, in the present rough cells, only observable for $A = 40$ mm and around $\tau_m/T \sim 1.3$. This implies that disorder introduced by the obstacles has only a small influence on the different types of Taylor dispersion: their characteristics are indeed mostly determined by the velocity profile and by transverse molecular diffusion which are both weakly influenced by the roughness of the walls.

In the following, we discuss therefore only novel results obtained at low Péclet numbers for which geometrical dispersion associated with the disorder of the velocity field (due to the wall roughness) is dominant. Geometrical dispersion depends very much on the distribution of the characteristic scales and spatial correlation of the flow heterogeneities induced by the roughness (Bear 1972). Oscillating flows are particularly well suited to analyze such structures because one can vary independently the amplitude A of the oscillations (i.e., the distance explored along the mean flow) and their period T and number N. One may, for instance, keep A constant while increasing the total distance travelled by the front.

A major issue in the interpretation of these measurements is the reversibility of tracer or front spreading with respect to flow reversals. A similar problem has been investigated previously in different porous media by means of echo dispersion measurements (Hulin and Plona 1989) in which there is only one injection–suction cycle. The degree of reversibility may be estimated by comparing the transmission and echo dispersivities (for instance for equal durations T_{inv} of the injection and suction phases in order to have equal flow paths in both directions). The result are very different depending on whether one deals with homogeneous media (i.e., correlation length of the flow heterogeneities small compared to the sample size) or with heterogeneous ones with large-scale heterogeneities. In the first case, transmission and echo dispersivities become equal above a very short path length x_{tr} (Rigord et al. 1990; Borgne et al. 2013, 2015; Anna et al. 2014; Jha et al. 2006, 2009). In the present case, Fig. 9 shows that there are low- and high-velocity channels of macroscopic width $\Delta W \gtrsim 10$ mm so that we deal with a strongly heterogeneous medium.

A simplified case of such heterogeneities is provided by media with strata of different permeabilities parallel to the flow (Leroy et al. 1992); if there is no tracer exchange between them, transmission dispersion is determined by the velocity contrasts between the strata and is generally not Gaussian. The effect of the contrasts cancels out in echo experiments because, at $t > T_{\text{inv}}$, the fluid particles follow backwards at the same velocity the same macroscopic paths as for $t > T_{\text{inv}}$: then, the echo dispersivity is much smaller than the transmission one. In real samples there is always some exchange between layers by transverse molecular diffusion or dispersion which reduces the effects of the velocity contrast. Transmission dispersivity is still larger than echo dispersivity, but the difference is smaller and depends on the transverse size of the heterogeneities, the Péclet number and on transverse diffusion/dispersion. Such

characteristics have been observed previously in model stratified media (Leroy et al. 1992) and natural rock samples (Hulin and Plona 1989). In the present medium, the first oscillation is equivalent to an echo experiment with $T_{\text{inv}} = T/2$. One observes indeed that the effective dispersivity is much larger at $t = T/2$ than at $t = T$, as expected by analogy with the above results.

An important additional feature of oscillating flow measurements is that they allow one to enhance the effect of transverse dispersion or diffusion by increasing the number N of the oscillations while keeping A constant. The variation with the travelled distance $x_{tr} = 4At/T$ of the instantaneous dispersivity l_d^{osc} is shown in Fig. 10. In the injection and suction phase of the first oscillation, one retrieves, as expected, values of the same order of magnitude as l_d^{inj} and l_d^{eco}, respectively. Then, the value of l_d oscillates with an amplitude decreasing with the distance and tends toward a constant value $l_{d\infty}^{\text{osc}}$: it represents the final irreversible component of dispersion after a large number of oscillations when transverse dispersion has allowed the tracer to reach a quasi-stationary transverse distribution.

The present experiments show that tracer dispersion in oscillating flows provides a broad variety of information on the mechanisms and degree of reversibility of dispersion. It is a sensitive and powerful approach for characterizing the heterogeneity of porous media which has very important practical applications to the study of pollutant propagation, chemical reactions in catalytic beds or separation processes It complements other techniques such as transmission and echo dispersion, for instance by using the number of oscillations and their amplitude for investigating the influence of different heterogeneity scales and transverse dispersion distances.

The model used in the present work is a simple representation of a rough fracture, and the same measurement technique may be applied to natural 3D porous media, fractures or milli- or microfluidic circuits. In small microfluidic circuits, oscillating allows one to increase the residence time within these circuits (and their effectiveness) without increasing their size. The present study has been restricted to the dispersion of a passive tracer, but the oscillating flow technique can also be applied to the flow of reactive species. Interesting issues are, for instance, the influence of oscillation on the dynamics of processes studied such as biodegradation or sorption. Applications to the improvement in mixing processes are also to be envisioned.

Acknowledgements We acknowledge support by "Investissements d'Avenir" LabEx PALM (ANR-10-LABX-0039-PALM), by the LIA PMF-FMF (Franco-Argentinian International Associated Laboratory in the Physics and Mechanics of Fluids) and from UBACyT 20020130100570BA. The thesis of Y. L. Roht has been supported by a fellowship from the Peruilh foundation of the Faculty of Engineering of the Buenos-Aires University, by a Bec.Ar fellowship and by an Eiffel fellowship. The authors wish to thank A. Aubertin, L. Auffray and R. Pidoux for their help in the design and realization of the experimental setup.

References

Aris, R.: On the dispersion of a solute in a fluid flowing through a tube. Proc. R. Soc. Lond. A **235**, 67–77 (1956)

Ashorynejad, H.R., Javaherdeh, K., Van den Akker, H.E.A.: The effect of pulsating pressure on the performance of a PEM fuel cell with a wavy cathode surface. Int. J. Hydrogen Energy **41**, 14239–14251 (2016)

Bear, J.: Dynamics of Fluids in Porous Media. Dover Publications, New-York (1972)

Boschan, A., Auradou, H., Chertcoff, R., Ippolito, I., Hulin, J.P.: Miscible displacement fronts of shear thinning fluids inside rough fractures. Water Resour. Res. **43**, W03438 (2007)

Boschan, A., Ippolito, I., Chertcoff, R., Auradou, H., Hulin, J.P.: Geometrical and Taylor dispersion in a fracture with random obstacles: an experimental study with fluids of different rheologies. Water Resour. Res. **44**, W06420 (2008)
Charette, V.J., Evangelista, E., Chertcoff, R., Auradou, H., Hulin, J.P., Ippolito, I.: Influence of the disorder on solute dispersion in a flow channel. Eur. Phys. J. Appl. Phys. **39**, 267–274 (2007)
Cirkel, D.G., van der Zee, S., Meeussen, J.C.L.: Front spreading with nonlinear sorption for oscillating flow. Water Resour. Res. **51**, 2986–2993 (2015)
de Anna, P., Dentz, M., Tartakovsky, A., Le Borgne, T.: The filamentary structure of mixing fronts and its control on reaction kinetics in porous media flows. Geophys. Res. Lett. **41**, 4586–4593 (2014)
Dey, B., Raja, G.P.: Sekhar "Mass transfer and species separation due to oscillatory flow in a Brinkman medium". Int. J. Eng. Sci. **74**, 35–54 (2014)
Fried, J.J., Combarnous, M.A.: Dispersion in Porous Media. In: Ven Te Chow (ed.) Advances in Hydroscience, pp. 1 69–282. Academic Press, New York (1971)
Horobin, R.W., Kiernan, J.A.: Conn's Biological Stains: A Handbook of Dyes, Stains and Fluorochromes for Use in Biology and Medicine. Taylor and Francis, Philadelphia (2002)
Hulin, J.P., Plona, T.J.: Echo tracer dispersion in porous media. Phys. Fluids A **1**, 1341–1347 (1989)
Ippolito, I., Daccord, G., Hinch, E.J., Hulin, J.P.: Echo tracer dispersion in model fractures with a rectangular geometry. J. Contam. Hydrol. **16**, 87–108 (1994)
Jha, R.K., Bryant, S.L., Lake, L.W., John, A.: Investigation of pore-scale (local) mixing. In: Paper SPE 99782 presented at the SPE Improved Oil Recovery Symposium, Tulsa (2006)
Jha, R.K., John, A., Bryant, S.L., Lake, L.W.: Flow reversal and mixing. SPE J. **14**, 41–49 (2009)
Le Borgne, T., Dentz, M., Villermaux, E.: Stretching, coalescence, and mixing in porous media. Phys. Rev. Lett. **110**, 204501 (2013)
Le Borgne, T., Dentz, M., Villermaux, E.: The lamellar description of mixing in porous media. J. Fluid Mech. **770**, 458–498 (2015)
Leong, K.C., Jin, L.W.: Characteristics of oscillating flow through a channel filled with open-cell metal foam. Int. J. Heat Fluid Flow **27**, 144–153 (2006)
Leroy, C., Hulin, J.P., Lenormand, R.: Tracer dispersion in stratified porous media: influence of transverse dispersion and gravity. J. Contam. Hydrol. **11**, 51–68 (1992)
Nowamooz, A., Radilla, G., Fourar, M., Berkowitz, B.: Non-Fickian transport in transparent replicas of rough-walled rock fractures. Transp. Porous Med. **98**, 651–682 (2013)
Raats, P.A.C.: Effect of a finite response time upon propagation of sinusoidal oscillations of fluids in porous media. Z. Angew. Math. Phys. **20**, 936–946 (1969)
Rigord, P., Calvo, A., Hulin, J.P.: Transition to irreversibility for the dispersion of a tracer in porous media. Phys. Fluids A **2**, 681–687 (1990)
Roht, Y.L., Auradou, H., Hulin, J.-P., Salin, D., Chertcoff, R., Ippolito, I.: Time dependence and local structure of tracer dispersion in oscillating liquid Hele-Shaw flows. Phys. Fluids **27**, 103602 (2015)
Roux, S., Plouraboué, F., Hulin, J.P.: Tracer dispersion in rough open cracks. Transport Porous Med. **32**, 97–116 (1998)
Russel, W.B., Saville, D.A., Schowalter, W.R.: Colloidal Dispersions. Cambridge University Press, Cambridge (1995)
Saffman, P.G.: A theory of dispersion in porous media. J. Fluid Mech **6**, 321–349 (1959)
Sanz-Prat, A., Lu, C., Finkel, M., Cirpka, O.A.: Using travel times to simulate multi-dimensional bioreactive transport in time-periodic flows. J. Cont. Hydro. **187**, 1–17 (2016)
Scotter, D.R., Raats, P.A.C.: Dispersion in porous mediums due to oscillating flow. Water Resour. Res. **4**, 1201–1206 (1968)
Scotter, D.R., Thurtell, G.W., Raats, P.A.C.: Dispersion resulting from sinusoidal gas flow in porous materials. Soil Sci. **104**, 306–308 (1967)
Taylor, G.I.: Dispersion of soluble matter in solvent flowing slowly through a tube. Proc. R. Soc. Lond. A **219**, 186–203 (1953)
Wang, P., Chen, G.Q.: Environmental dispersion in a tidal wetland with sorption by vegetation. Commun. Nonlinear Sci. Numer. Simulat. **22**, 348–366 (2015)
Watson, E.J.: Diffusion in oscillatory pipe flow. J. Fluid. Mech. **133**, 233–244 (1983)